Modelling of an InAs/GaSb/InSb short-period superlattice laser diode for mid-infrared emission by the k.p method

2010 J. Phys. D: Appl. Phys. 43 325102

(http://iopscience.iop.org/0022-3727/43/32/325102)

IOP PUBLISHING JOURNAL OF PHYSICS D: APPLIED PHYSICS

J. Phys. D: Appl. Phys. **43** (2010) 325102 (7pp) doi:10.1088/0022-3727/43/32/325102

Modelling of an InAs/GaSb/InSb short-period superlattice laser diode for mid-infrared emission by the k.p method

S Ben Rejeb[1], M Debbichi[1,3], M Said[1,3], A Gassenq[2], E Tournié[2] and P Christol[2]

[1] Unité de recherche de Physique des Solides, Département de Physique, Faculté des Sciences de Monastir, 5019 Monastir, Tunisia

[2] Institut d'Electronique du Sud (IES), UMR CNRS 5214, Case 067, Université Montpellier 2, 34 095 Montpellier cedex 05, France

E-mail: mourad_fsm@yahoo.fr and moncef_said@yahoo.fr

Received 23 May 2010, in final form 29 June 2010
Published 23 July 2010
Online at stacks.iop.org/JPhysD/43/325102

Abstract

The electronic band structure and optical gain of an InAs/GaSb/InSb short-period superlattice laser diode on a GaSb substrate are numerically investigated with an accurate 8×8 k.p model. Using a realistic graded and asymmetric interface profile, we obtain a reasonable agreement on band gap energy with our experimental data extracted from laser emissions performed on the laser diode. The optical performance in terms of optical gain is then calculated for the laser structure and we demonstrate the utility of interface design to model short-period superlattice structures.

1. Introduction

Antimonide-based systems show great potential for photonic devices in a wide wavelength range, including the useful 3–5 μm mid-infrared atmospheric window. In combination with InAs binary, antimonides (Sb) can form type-II broken-gap band alignment (also called type-III). These types of heterostructures are particularly relevant because of the expected suppression of non-radiative Auger recombinations in such designs [1]. One material system that shows promise for emission at ambient temperature is $(InAs)_n/(GaSb)_m$ superlattices (SLs) on GaSb substrates [2]. The use of these SLs for mid-infrared lasers and photodetectors depends not only on the successful growth of the periodic structures but also on the accurate design of their band gaps. Indeed, in InAs/GaSb SLs, the heterointerface presents a type-II broken-gap alignment wherein the valence band of GaSb is about 150 meV above the conduction band of InAs [3], making interband optical transitions between the confined electron and hole miniband states possible. Consequently, in this system, the layer thicknesses control the separation of the confined states and the InAs/GaSb SL effective band gap can be tuned to the mid-IR by adjusting InAs and GaSb layer thicknesses [4]. However, the physical properties such as band offset [5] and device performance [6] are critically dependent on the composition and structure of interfaces. Using cross-sectional scanning tunnelling microscopy (STM), Steinshnider *et al* have highlighted different types of interfacial bonds that occur in SLs [7]. Previous studies demonstrate that InAs/GaSb [8], AlAs/GaAs [9] and InAs/GaAs [10] SLs are known to have interfaces that are not always abrupt, but show some concentration profiles due to the tendency of the anion and cation atoms to intermix. This effect due to the difference in surface energies of the various components of the materials causes certain atomic species to segregate to the surface during growth and leads to structural and chemical asymmetries in the compositional profiles of SLs.

The electronic and optical properties of InAs/GaSb SLs have been found to depend mainly on the monolayer sequence at the interfaces (IFS) [11, 12]. There are a number of experimental reasons to consider the interfacial morphology of such SLs due to the well-known tendency of Sb to surface segregate relative to As and the tendency of In to surface segregate relative to Ga. These effects induced possible disorder effects on interfacial morphology and affected the electronic properties [13, 14]. This property has recently been

[3] Authors to whom any correspondence should be addressed.

observed by cross-sectional STM measurements on InAs/GaSb SLs where possible Sb penetration into the first few InAs monolayers was identified [15].

The k.p method within the envelope-function approximation (EFA) has been widely used in modelling quantum wells, quantum dots and large period SLs, in particular for electronic states close to the Γ point of the Brillouin zone. However, this method has not been successful in describing the electronic structure of such short-period superlattices (SPSLs), in particular if they are assumed to be abrupt [16]. The atomistic calculations such as the pseudopotential techniques have often been suggested as more accurate alternatives to the standard model (EFA) [8, 12, 13, 17].

The k.p method assumes equal Bloch functions in the well and the barrier of the heterostructures due to the lack of a common atom at the interfaces between the two materials. To overcome these difficulties, some modifications to the k.p method have been proposed, such as the modified EFA model which describes the interface interaction in $(InAs)_n/(GaSb)_m$ SPSL using short-range delta function potentials at the centre of the interface InAs–GaSb [4, 11], or the use of an interface profile (graded and asymmetric interface) that seems to be more realistic with experimental observations [14]. In this framework of approximation, the modified EFA has been successfully used to describe the evolution of the fundamental interminiband transition energy and absorption spectra of SPSL-based structures, giving good agreement with the experimental data [2, 14].

In order to reduce the natural tensile strain of the InAs layer on GaSb, it is well known that intentional insertion of highly strained ($\varepsilon = 6.3\%$) InSb layer in each SPSL's period has to be considered [18] for the fabrication of high-quality samples.

The objective of this work is to study the electronic and optical properties of a strained InAs/GaSb/InSb SPSL structure suitable for a laser diode.

This paper is organized as follows. Section 2.1 explains the 8×8 k.p Hamiltonian used for the valence and conduction bands levels for the determination of the fundamental energy gap and dispersion relations of the SPSL while an optical gain relation is given in section 2.2. The SPSL as an active zone of the laser structure is described in section 3.1 while a discussion on the results obtained is presented in section 3.2.

2. Theoretical considerations

2.1. Band structure calculation

To calculate the band structure, electrons and holes wavefunctions of the SPSL near the Brillouin zone, an eight-band k.p model within the EFA is used.

The 8-band Hamiltonian for a strained bulk semiconductor, which takes into account the energy levels from conduction, heavy-hole, light-hole and spin–orbit split-off bands, in the bases $|S\uparrow\rangle, |S\downarrow\rangle, \left|\frac{3}{2}\right\rangle, \left|\frac{1}{2}\right\rangle, \left|-\frac{1}{2}\right\rangle, \left|-\frac{3}{2}\right\rangle, \left|\frac{7}{2}\right\rangle, \left|-\frac{7}{2}\right\rangle$ has been described in our recent works [19, 20].

Using an appropriate basis set and taking into account the effects of strain, the 8×8 Hamiltonian is diagonalized into [21]

$$H_{8\times8}(k_\rho) = \begin{pmatrix} H^{+}_{4\times4}(k_\rho) & 0 \\ 0 & H^{-}_{4\times4}(k_\rho) \end{pmatrix}, \tag{1}$$

where the upper and lower blocks $H^{+}_{4\times4}$ and $H^{-}_{4\times4}$ are given by

$$H^{\mp}_{4\times4}(k_\rho) = \begin{bmatrix} f & \mp g & \mp\frac{g}{\sqrt{3}} - h & \mp\sqrt{\frac{2}{3}}g + \frac{h^*}{\sqrt{2}} \\ \mp g & a_+ & c \mp \mathrm{i}b & \sqrt{2}c \pm \mathrm{i}\frac{b}{\sqrt{2}} \\ \mp\frac{g}{\sqrt{3}} + h^* & c \pm \mathrm{i}b & a_- & -e \pm \mathrm{i}\sqrt{\frac{3}{2}}b \\ \mp\sqrt{\frac{2}{3}}g - \frac{h}{\sqrt{2}} & \sqrt{2}c \mp \mathrm{i}\frac{b}{\sqrt{2}} & -e \mp \mathrm{i}\sqrt{\frac{3}{2}}b & d \end{bmatrix}. \tag{2}$$

Taking the zero of energy at the top of the valence band, the matrix elements are

$$f = E_\mathrm{g} + \tilde{\gamma}_c\tilde{k}^2 + \delta E_\mathrm{c}^\mathrm{hy},$$

$$a_\pm = -\tilde{\gamma}_1\tilde{k}^2 \pm \tilde{\gamma}_2(2\tilde{k}_z^2 - \tilde{k}_\rho^2) + \delta E_\mathrm{v}^\mathrm{hy} \pm \zeta,$$

$$d = -\Delta - \tilde{\gamma}_1\tilde{k}^2 + \delta E_\mathrm{v}^\mathrm{hy},$$

$$b = 2\sqrt{3}\tilde{\gamma}_3\tilde{k}_\rho k_z,$$

$$e = \sqrt{2}(2\tilde{\gamma}_2\tilde{k}_z^2 - \tilde{\gamma}_2\tilde{k}_\rho^2),$$

$$g = \frac{1}{\sqrt{2}}Pk_\rho,$$

$$h = \sqrt{\frac{2}{3}}\mathrm{i}Pk_z,$$

$$c = \sqrt{3}\frac{(\tilde{\gamma}_2 + \tilde{\gamma}_3)}{2}\tilde{k}_\rho^2,$$

$$\tilde{\gamma}_c = \frac{1}{m_\mathrm{c}^*} - \frac{E_\mathrm{p}}{3}\left[\frac{2}{E_\mathrm{p}} + \frac{1}{E_\mathrm{g} + \Delta}\right],$$

where the wave vectors are defined by

$$k_\rho = \sqrt{k_x^2 + k_y^2}, \qquad k^2 = k_\rho^2 + k_z^2,$$

$$\tilde{k}_j^2 = \frac{\hbar^2}{2m_0}k_j^2, \quad j = x, y, z.$$

Here, m_0 is the free-electron mass; $\tilde{\gamma}_1$, $\tilde{\gamma}_2$ and $\tilde{\gamma}_3$ are the modified Luttinger parameters, Δ is the magnitude of spin–orbit splitting at $k_\rho = 0$ and $E_\mathrm{p} = (2m_0P^2)/\hbar^2$ is the Kane energy related to the Kane matrix element P [19].

$\delta E_\mathrm{c,v}^\mathrm{hy} = -2a_\mathrm{c,v}(1 - c_{12}/c_{11})\varepsilon_{xx}$ and $\zeta = -b_\mathrm{v}(1 + 2c_{12}/c_{11})\varepsilon_{xx}$ describe the influence of hydrostatic and shear strain components on the band structure, where $a_\mathrm{c,v}$ are the hydrostatic deformation potentials for conduction and valence bands, respectively; c_{11} and c_{12} are the elastic constants, b_v is

the axial deformation potential and ε_{xx} is the strain in the layer plane.

Using the finite-difference method, the energies and envelope functions of electron and valence subbands can be obtained by numerically solving the multi-band effective-mass equations:

$$\sum_{\nu'=1,4}\left[H^{+}_{\nu\nu'}\left(k_\rho, -\mathrm{i}\frac{\mathrm{d}}{\mathrm{d}z}\right) + V(z)\delta_{\nu\nu'}\right]F_n^{(\nu')}(k_\rho, z)$$
$$= E_n(k_\rho)F_n^{(\nu')}(k_\rho, z)$$

and

$$\sum_{\nu'=1,4}\left[H^{-}_{\nu\nu'}\left(k_\rho, -\mathrm{i}\frac{\mathrm{d}}{\mathrm{d}z}\right) + V(z)\delta_{\nu\nu'}\right]F_n^{(\nu'+4)}(k_\rho, z)$$
$$= E_n(k_\rho)F_n^{(\nu'+4)}(k_\rho, z), \qquad \nu = \{1, 2, 3, 4\}, \tag{3}$$

where $F_n^{\nu'}$ is the envelope function and $V(z)$ the unstrained quantum-well potential.

After discretizing the coupled differential equations (2), the problem is reduced to an eigenvalue problem to be solved for the subband energies $E_n(k_\rho)$ and the discretized envelope functions. A detailed description of the finite-difference method is given in the appendix.

2.2. Optical gain

The optical performance of a SPSL (InAs/GaSb/InSb) laser structure is estimated in terms of optical gain in TE mode polarization, with an intraband relaxation time of 10^{-13} s [20].

The optical gain at phonon energy $\hbar\omega$ is calculated by the following relation [22]:

$$G(\omega) = \frac{e^2}{n_\mathrm{r}c\varepsilon_0 m_0^2\omega L_\mathrm{eff}}\sum_{n,m}\int_0^\infty |\widehat{e}.M_{n,m}(k_\rho)|^2\{F_\mathrm{c}^n[E_\mathrm{c}^n(k_\rho)]$$
$$- F_\mathrm{v}^m[E_\mathrm{v}^m(k_\rho)]\}\frac{k_\rho\,\mathrm{d}k_\rho}{2\pi} \times L[E_{\mathrm{c,v}}^{n,m}(k_\rho)], \tag{4}$$

where

$$L[E_{\mathrm{c,v}}^{n,m}(k_\rho)] = \frac{\hbar/\tau_\mathrm{int}}{[E_\mathrm{c}^n(k_\rho) - E_\mathrm{v}^m(k_\rho) - \hbar\omega]^2 + (\hbar/\tau_\mathrm{int})^2},$$

c and ε_0 are the velocity of light and permittivity of free space, n_r and L_eff are the refractive index and the effective width of the active zone, respectively. F_c^n and F_v^m are the Fermi functions for the mth subband in the valence band (holes) and the nth subband in the conduction band, respectively, and τ_int is the intraband relaxation time.

$|\widehat{e}.M_{n,m}(k_\rho)|$ is the optical transition matrix element between the hole subbands and the electron subbands. The final expression for the squared optical matrix is detailed in [23].

3. Results and discussion

3.1. SPSL laser structure design

The designed SPSL structure is made of N periods (4 ML-InAs/3 ML-GaSb/1 ML-InSb/3 ML-GaSb), where 1 ML represents one monolayer (i.e. ∼3 Å in this materials system), which are in turn surrounded by 100 Å thick AlGaAsSb barriers lattice-matched to the GaSb substrate. Such a SPSL active zone is appropriate for emission in the 3–4 μm wavelength range.

The structure with a segregated profile is obtained by introducing an interface layer that comprises 2 MLs of material with graded composition, of which 1 ML is taken from GaSb and the other from InAs. This material is the quaternary $Ga_xIn_{1-x}As_{1-y}Sb_y$ where x and y may be independent. For simplicity we use $(InAs)_x(GaSb)_{1-x}$ as the interface layer. This interface layer is constructed on the basis of the different dominating interface-disorder mechanisms for the two interfaces, GaSb on InAs and InAs on GaSb [10, 14].

Figure 1 shows the schematic band diagram with the fundamental electron e1, heavy hole hh1 and light hole lh1 levels and their relative wavefunctions for $N = 30$ periods of the SPSL active region relative to the abrupt interfaces.

The energies and wavefunctions of holes and electrons of the SPSL are calculated in the framework of the method mentioned above in section 2. The material parameters used are given in table 1. The unstrained conduction and valence band offset ΔE_c and ΔE_v were calculated by interpolating binary heterointerface values from table 2. We choose the quantum well direction (z-axis) as the quantization of angular momentum.

3.2. SPSL laser structure results

To clarify the relative role of interface bonding and compositional gradients, we plot in figure 2(a) the fundamental energy gap as a function of the number of periods N for the abrupt and segregated interfaces. For N periods lower than 15, whatever the approximation, we can observe a strong variation in the calculated emission energy which is a signature of multi-quantum well behaviour. For a higher N value we can see that the number of periods does not significantly affect the emission energy, which is a mark of the SPSL structures with the SL effect and the presence of energy minibands [25].

On the other hand, in the case of interface interaction, the segregated composition profile induces a decrease in the transition energy values between 30% and 40%, giving a reasonable agreement with our experimental data extracted from the PL spectra reported in figure 2(b). This result proves the applicability of the multi-band k.p in modelling the InAs/GaSb/InSb SPSL structure.

To clarify the origin of the physical behaviour by which the graded composition profile affects the optical transition energy, a focus on theoretical results is given in figure 3, where the fundamental subband energy levels of conduction (figure 3(a)) and valence (figure 3(b)) bands as a function of the number of periods N are plotted. In addition, we have plotted in figure 4 the modification of the potential profiles for the conduction band (CB) and the heavy-hole valence band (VB). One can see that the quantum-well profile for the electrons in the graded interface is wider than for the abrupt interfaces, causing a decrease in the size-quantization energy for an electron miniband of 130 meV. Similarly, the quantum-well profile for holes in the graded structure is narrower.

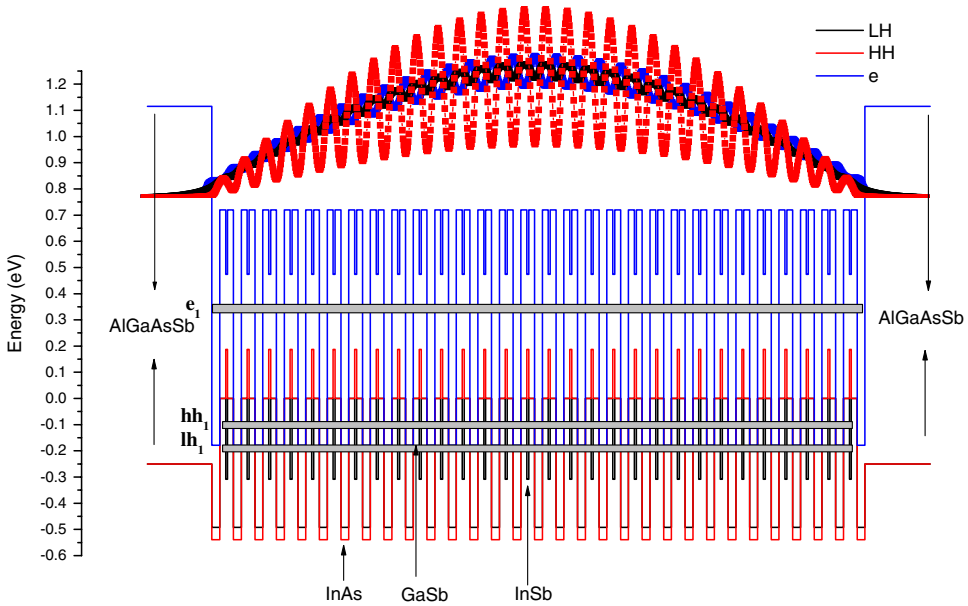

Figure 1. Band profiles, energy levels and wavefunction of fundamental electron e1, heavy hole hh1 and light hole lh1 levels for abrupt 30-period InAs (4 ML)/GaSb (3 ML)/InSb (1 ML)/GaSb (3 ML) structure.

(This figure is in colour only in the electronic version)

Table 1. Physical parameters used in modelling at 300 K.

Parameters	Symbols	InAs	GaSb	AlAs	AlSb	InSb	GaAs
Lattice constant	a (Å)	6.0584	6.0954	5.6622	6.1355	6.4794	5.6532
Band Gap	E_g (eV)	0.356	0.725	3.099	2.386	0.172	1.519
Electron mass	m_e^*/m_0	0.023	0.042	0.15	0.14	0.0136	0.0665
Luttinger parameters	γ_1	20.4	13.3	3.4	4.15	36.27	6.85
	γ_2	8.5	4.4	0.82	1.19	15.5	2.1
	γ_3	9.2	6.0	1.42	1.97	16.5	2.93
Deformation potentials	a_v (eV)	1.00	0.8	2.47	1.38	0.36	1.16
	a_c (eV)	−5.08	−7.5	−5.64	−6.97	−6.17	−7.17
	b (eV)	−1.8	−2.0	−1.5	−1.4	−2.1	−1.70
Elastic constant	C_{11} (GPa)	832.9	884.2	1250	876.9	684.7	1221
	C_{12} (GPa)	452.6	402.6	534	434.1	373.5	566
Spin–orbit energy	Δ_0 (eV)	0.39	0.76	0.28	0.676	0.81	0.341
Kane potential	E_p (eV)	21.11	22.88	21.10	18.70	23.3	22.71

Table 2. Valence band offset ΔE_v (eV) between unstrained III–V systems [24].

Systems	ΔE_v (eV)	Potential profile
InAs/GaSb	−0.51	Type-III
InAs/InSb	−0.43	Type-III
InAs/AlSb	−0.11	Type-II
InAs/AlAs	0.65	Type-I
InAs/GaAs	0.17	Type-I

Our calculations show that the overall effect caused by the segregated interface profile on the heavy-hole miniband is low, inducing a shift of about 35 meV. This shift in energy of electron and hole minibands is a direct consequence of the physical asymmetry in the composition profile at the interfaces due to different dominating interface-disorder mechanisms for GaSb on InAs and InAs on GaSb.

Figure 5 plots the in-plane dispersion curve for the typical electron and valence bands calculated using the method mentioned above for 30-period 4 ML-InAs/3 ML-GaSb/1 ML-InSb/3 ML-GaSb SPSLs with band profiles for abrupt (solid line) and segregated (dashed line) interfaces. The claddings consist of $Al_{0.9}Ga_{0.1}As_{0.07}Sb_{0.93}$ which is lattice-matched to the GaSb substrate. This structure is designed to operate in the 3.7 μm range when the interfaces effect is added. In our coordinate system, zero energy is the hole band-edge energy of InSb.

At $k_\rho = 0$, where k_ρ is the wave vector in the plan direction, heavy and light holes are exactly decoupled and their corresponding energies for the upper (H^+) and lower (H^-) block Hamiltonian are degenerate. So, it is possible to label subbands as 'heavy hole' or 'light hole' according to their main character at the Γ point. Also noted on these graphs is the order of the subbands as e1, e2, hh1, hh2, lh1, lh2, hh3, etc. For a nonzero k_ρ, the increasing admixture of holes, electron and spin–orbit functions into holes, electron and spin–orbit states gives rise to strong nonparabolicities in the valence band structure which lead particularly to a remarkable

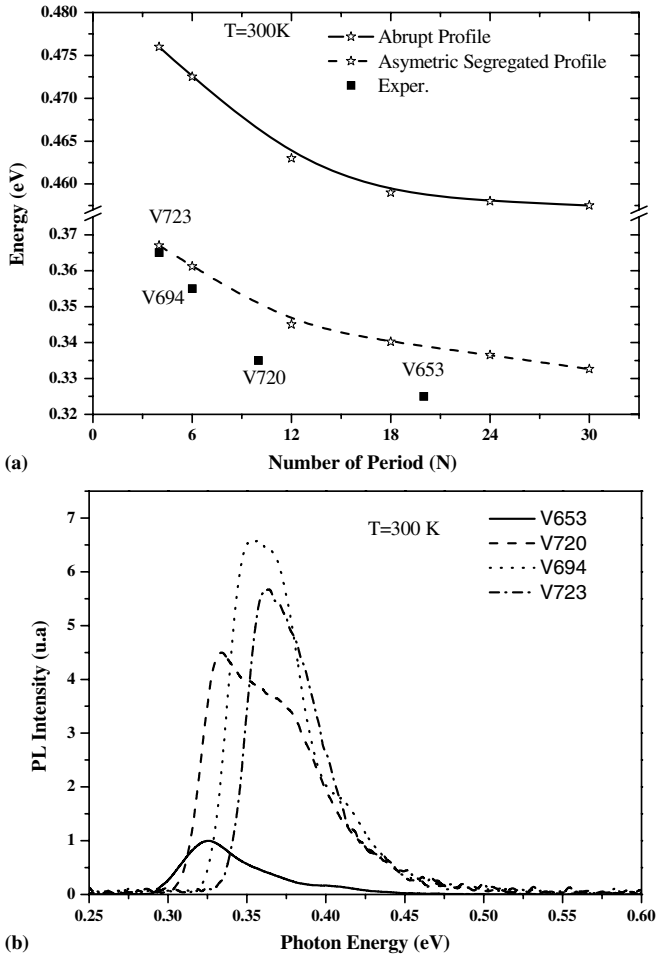

Figure 2. (*a*) Fundamental gap of SPSL (4 ML-InAs/3 ML-GaSb/1 ML-InSb/3 ML-GaSb)$_N$ for the abrupt and segregated profiles at room temperature compared with experimental data (solid squares) extracted from PL spectra. (*b*) Room temperature photoluminescence (PL) emission spectra of SPSL structures. The samples were optically pumped with a 784 nm fibre-coupled GaAs laser diode (0.5 kW cm^2) and PL signal measurements were collected by a Nicolet 870 Nexus Fourier transform infrared (FTIR) spectrometer using an InSb detector.

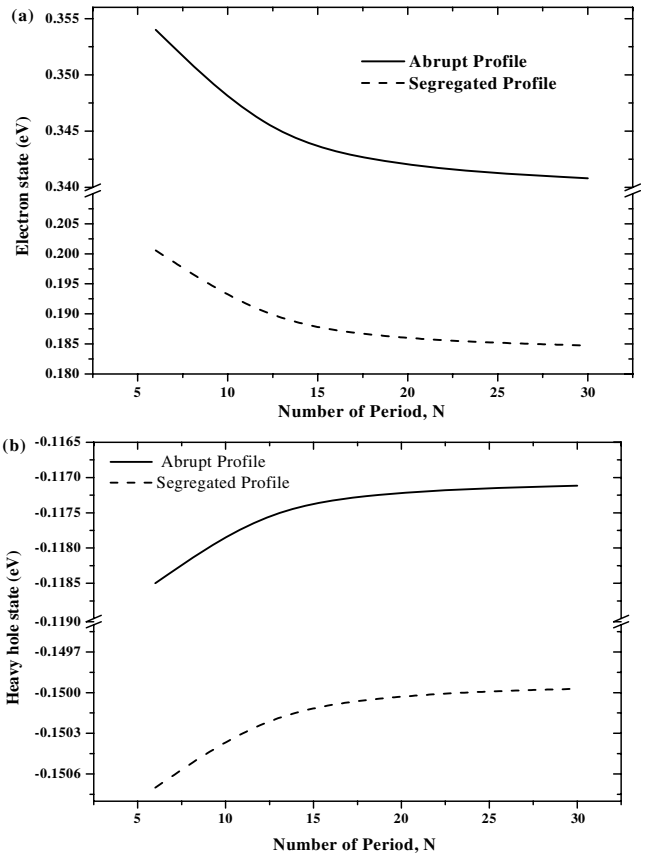

Figure 3. Fundamental subband energy levels from conduction e1 (*a*) and valence hh1 (*b*) bands as a function of the number of periods.

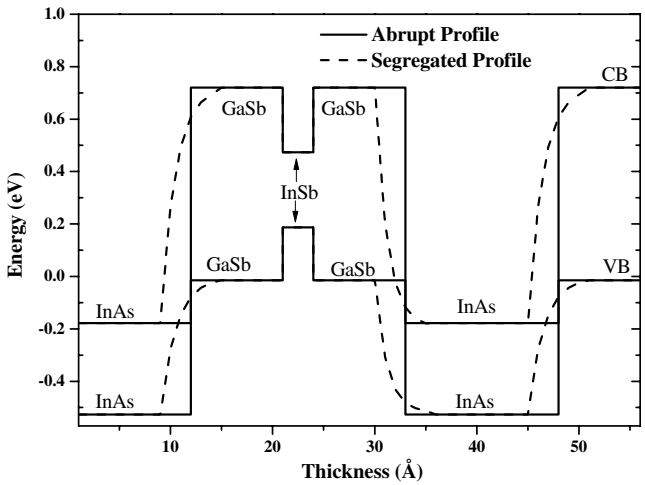

Figure 4. A schematic representation of band profile for the abrupt (solid line) and segregated interfaces (dashed line).

anticrossing behaviour for the excited levels lh2, hh3 and lh3 at about $k_\rho \sim 0.046$ Å^{-1}.

For the abrupt profile, at a critical wavevector $k_\rho \sim 0.01$ Å^{-1} the hole states lh1 and hh2 give a crossing, demonstrating the strong mixing. However, this effect is not present in the segregated profile due to the limited spatial overlap of the hh2 and lh1 states.

For the conduction band, segregation affects mainly the first level e1 inducing a large enhancement of transition energy between the first two conduction subbands e2-e1.

We now apply the potential profile of the InAs/GaSb interfaces to calculate the optical gain at room temperature of the midwave infrared (MWIR) SPSL (30-period 4 ML-InAs/3 ML-GaSb/1 ML-InSb/3 ML-GaSb) using equation (4). Figure 6 shows the optical gain spectrum for normal incidence (transverse electric (TE)) calculated for segregated interfaces. For carrier injections increasing from 0.5×10^{19} to 2×10^{19} cm^{-3}, the conduction subbands e1 and e2 and the valence subbands hh1 and hh2 are occupied, thus, the transition e2–hh2 appears at the gain spectrum. A gain value of around 1300 cm^{-1} is reached with a typical injected carrier density of 2×10^{19} cm^{-3}. This value is higher than those obtained on a InAs/GaSb SPSL laser structure adapted for MWIR emission at room temperature [14].

4. Conclusion

A new short-period InAs/GaSb/InSb SL structure has been modelled for emission in the mid-infrared range at

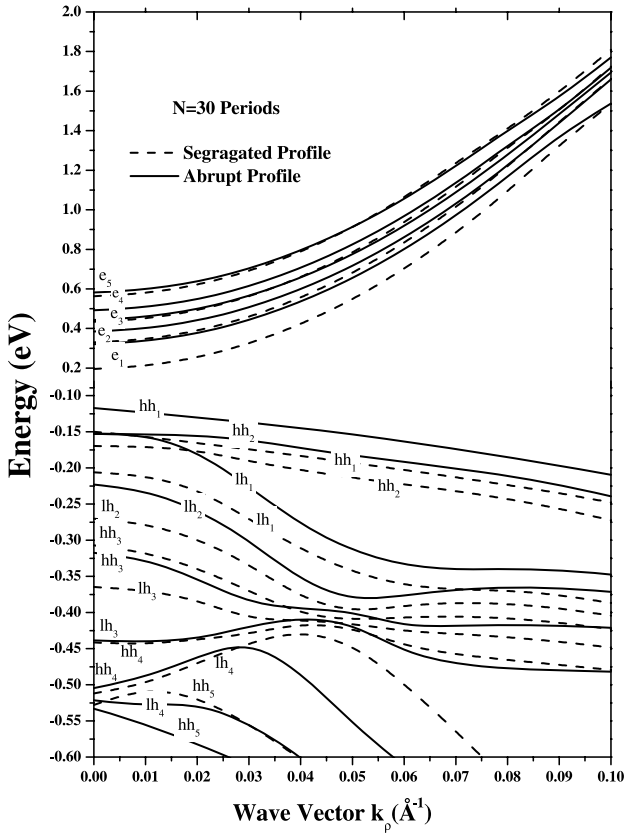

Figure 5. Band structure of 30-period (4 ML-InAs/3 ML-GaSb/1 ML-InSb/3 ML-GaSb) SPSL for the abrupt (solid line) and segregated (dashed line) profiles calculated with the eight-band k.p model.

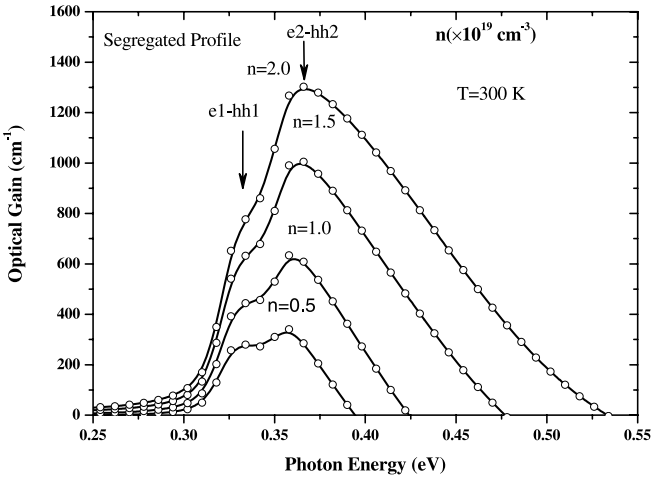

Figure 6. Gain spectrum (TE mode) versus photon energy in 30-period (4 ML-InAs/3 ML GaSb/1 ML-InSb/3 ML-GaSb) SPSL for different carrier injection densities.

room temperature using an accurate eight-band k.p method including interface interactions. Our results have shown that the asymmetric interfacial segregation modifies the size-quantization energy for the electron and hole minibands, leading to a reduction in the fundamental gap energy of about 30%, in agreement with our experimental data. Taking account of this approach, we have calculated the optical gain spectrum of the MWIR SPSL at room temperature and the maximum gain value obtained shows the possibility to reach room temperature operation. Overall, the present work demonstrates the applicability of the k.p method to model InAs/GaSb/InSb SPSLs and the utility of the interface design as a tool in band gap engineering to define MWIR SPSL structures.

Appendix

We describe the finite-difference method for the lower $H_{4\times4}^{-}$ block Hamiltonian given in section 2. From equations (1) and (2), we have four coupled differential equations for $F_n^{(1)}(k_\rho, z)$, $F_n^{(2)}(k_\rho, z)$, $F_n^{(3)}(k_\rho, z)$ and $F_n^{(4)}(k_\rho, z)$:

$$\begin{bmatrix} f & -g & -\frac{g}{\sqrt{3}} - h & -\sqrt{\frac{2}{3}}g + \frac{h^*}{\sqrt{2}} \\ -g & a_+ & c - \mathrm{i}b & \sqrt{2}c + \mathrm{i}\frac{b}{\sqrt{2}} \\ -\frac{g}{\sqrt{3}} + h^* & c + \mathrm{i}b & a_- & -e + \mathrm{i}\sqrt{\frac{3}{2}}b \\ -\sqrt{\frac{2}{3}}g - \frac{h}{\sqrt{2}} & \sqrt{2}c - \mathrm{i}\frac{b}{\sqrt{2}} & -e - \mathrm{i}\sqrt{\frac{3}{2}}b & d \end{bmatrix} \times \begin{bmatrix} F_n^{(1)}(k_\rho, z) \\ F_n^{(2)}(k_\rho, z) \\ F_n^{(3)}(k_\rho, z) \\ F_n^{(4)}(k_\rho, z) \end{bmatrix} = E_n(k_\rho) \begin{bmatrix} F_n^{(1)}(k_\rho, z) \\ F_n^{(2)}(k_\rho, z) \\ F_n^{(3)}(k_\rho, z) \\ F_n^{(4)}(k_\rho, z) \end{bmatrix}.$$

We define $\phi_{\mathrm{e}}(z) = F_n^{(1)}(k_\rho, z)$, $\phi_{\mathrm{h}}(z) = F_n^{(2)}(k_\rho, z)$, $\phi_{\mathrm{l}}(z) = F_n^{(3)}(k_\rho, z)$ and $\phi_{\mathrm{s}}(z) = F_n^{(4)}(k_\rho, z)$. Then the coupled differential equations for $\phi_{\mathrm{e}}(z)$, $\phi_{\mathrm{h}}(z)$, $\phi_{\mathrm{l}}(z)$ and $\phi_{\mathrm{s}}(z)$ with their strained potentials, respectively, are

$$\left[C_1 E_{\mathrm{g}} + \tilde{A} + A\frac{\mathrm{d}^2}{\mathrm{d}z^2} + C_1 V_{\mathrm{c}}\right]\phi_{\mathrm{e}}(z) - C_1 A_3 \phi_{\mathrm{h}}(z) - C_1\left[A_4 + A_5\frac{\mathrm{d}}{\mathrm{d}z}\right]\phi_{\mathrm{l}}(z) - C_1\left[A_6 - A_7\frac{\mathrm{d}}{\mathrm{d}z}\right]\phi_s(z) = \lambda\phi_{\mathrm{e}}(z), \tag{A.1}$$

$$-C_1 A_3 \phi_{\mathrm{e}}(z) + \left[-A_1 + A_2\frac{\mathrm{d}^2}{\mathrm{d}z^2} + C_1 V_{\mathrm{h}}(z)\right]\phi_{\mathrm{h}}(z) + \left[C_2 - D_1\frac{\mathrm{d}}{\mathrm{d}z}\right]\phi_{\mathrm{l}}(z) + \left[A_8 + A_9\frac{\mathrm{d}}{\mathrm{d}z}\right]\phi_{\mathrm{s}}(z) = \lambda\phi_{\mathrm{h}}(z), \tag{A.2}$$

$$C_1\left[-A_4 + A_5\frac{\mathrm{d}}{\mathrm{d}z}\right]\phi_{\mathrm{e}}(z) + \left[C_2 + D_1\frac{\mathrm{d}}{\mathrm{d}z}\right]\phi_{\mathrm{h}}(z) + \left[-B_1 + B_2\frac{\mathrm{d}^2}{\mathrm{d}z^2} + C_1 V_{\mathrm{l}}(z)\right]\phi_{\mathrm{l}}(z) + \left[A_{12}\frac{\mathrm{d}}{\mathrm{d}z} - A_{10}\frac{\mathrm{d}^2}{\mathrm{d}z^2} - A_{11}\right]\phi_{\mathrm{s}}(z) = \lambda\phi_{\mathrm{l}}(z), \tag{A.3}$$

$$-C_1\left[A_6 + A_7\frac{\mathrm{d}}{\mathrm{d}z}\right]\phi_{\mathrm{e}}(z) + \left[A_8 - A_9\frac{\mathrm{d}}{\mathrm{d}z}\right]\phi_{\mathrm{h}}(z)$$
$$+\left[A_{11} - A_{10}\frac{\mathrm{d}^2}{\mathrm{d}z^2} - A_{12}\frac{\mathrm{d}}{\mathrm{d}z}\right]\phi_{\mathrm{l}}(z)$$
$$+\left[-C_1\Delta_0 - A_{13} + A_{14}\frac{\mathrm{d}^2}{\mathrm{d}z^2} + C_1V(z)\right]\phi_{\mathrm{s}}(z) = \lambda\phi_{\mathrm{s}}(z), \tag{A.4}$$

where

$$A_1 = \frac{\tilde{\gamma}_1 + \tilde{\gamma}_2}{2}k_\rho^2, \quad A_2 = \frac{\tilde{\gamma}_1 - 2\tilde{\gamma}_2}{2}, \quad \bar{\gamma} = \frac{\tilde{\gamma}_2 + \tilde{\gamma}_3}{2},$$
$$B_1 = \frac{\tilde{\gamma}_1 - \tilde{\gamma}_2}{2}k_\rho^2, \quad B_2 = \frac{\tilde{\gamma}_1 + 2\tilde{\gamma}_2}{2}, C_1 = \frac{m_0}{\hbar^2},$$
$$A_3 = \frac{P}{\sqrt{2}}k_\rho, \quad A_4 = \frac{P}{\sqrt{6}}k_\rho, \quad A_5 = \sqrt{\frac{2}{3}}P,$$
$$A_6 = \frac{P}{\sqrt{3}}k_\rho, \quad A_7 = \frac{P}{\sqrt{3}}, \tilde{A} = \frac{\tilde{\gamma}_c}{2}k_\rho^2, \quad A = \frac{\tilde{\gamma}_c}{2},$$
$$C_2 = \frac{\sqrt{3}}{2}\bar{\gamma}k_\rho^2, \quad D_1 = \sqrt{3}\tilde{\gamma}_3k_\rho, \quad A_8 = \sqrt{\frac{3}{2}}\bar{\gamma}k_\rho^2,$$
$$A_9 = \sqrt{\frac{3}{2}}\tilde{\gamma}_3k_\rho^{'} \quad A_{10} = \sqrt{2}\tilde{\gamma}_2, \quad A_{11} = \frac{\tilde{\gamma}_2}{\sqrt{2}}k_\rho^2,$$
$$A_{12} = \frac{3\tilde{\gamma}_3}{\sqrt{2}}k_\rho, \quad A_{13} = \frac{\tilde{\gamma}_1}{2}k_\rho^2, \quad A_{14} = \frac{\tilde{\gamma}_1}{2} \quad \text{and} \quad \lambda = C_1E.$$

$V_{\mathrm{e,h,l,s}}(z)$ are the strained potentials for electron, heavy-hole, light-hole and spin–orbit bands.

Finally, one needs to discretize these equations, evaluate the coefficients $A_1, \ldots, A_{14}$ for each k_ρ and solve for the eigenvalue λ numerically. The same procedure will be applied to the upper block Hamiltonian $H_{4\times4}^{+}$.

References

[1] Bürkle L and Fuchs F 2002 *Handbook of Infrared Detection Technologies* ed M Henini and M Razeghi (London: Elsevier) p 159

[2] Gassenq A, Boissier G, Grech P, Narcy G, Baranov A N and Tournié E 2009 InAs/GaSb/InSb short-period super-lattice diode lasers emitting near 3.3 μm at room-temperature *Electron. Lett.* **45** 165–7

[3] Smith D L and Mailhiot C 1987 Proposal for strained type II superlattice infrared detectors *J. Appl. Phys.* **62** 2545

[4] Rodriguez J B, Christol P, Chevrier F and Joullié A 2005 Optical characterization of symmetric InAs/GaSb superlattices for detection in the 3–5 μm spectral region *Physica* E **28** 128–33

[5] Wang M W, Collins D A, McGill T C, Grant R W and Feenstra R M 1995 Effect of interface composition and growth order on the mixed anion InAs/GaSb valence band offset *Appl. Phys. Lett.* **66** 2981–3

[6] Shiralagi K, Shen J and Tsui R1997 Effects of layer design on the performance of InAs/AlSb/GaSb resonant interband tunneling diodes on GaAs substrates *J. Electron. Mater.* **26** 1417–21

[7] Steinshnider J, Weimer M, Kaspi R and Turner G W 2000 Visualizing interfacial structure at non-common-atom heterojunctions with cross-sectional scanning tunneling microscopy *Phys. Rev. Lett.* **85** 2953

[8] Magri R and Zunger A 2001 Effects of interfacial atomic segregation on optical properties of InAs/GaSb superlattices *Phys. Rev.* B **64** 081305

[9] Braun W, Trampert A, Däweritz L and Ploog K H 1997 Nonuniform segregation of Ga at AlAs/GaAs heterointerfaces *Phys. Rev.* B **55** 1689–95

[10] Moison J M, Guille C, Houzay F, Barthe F and Van Rompay M 1989 Surface segregation of third-column atoms in group III–V arsenide compounds: ternary alloys and heterostructures *Phys. Rev.* B **40** 6149–62

[11] Szmulowicz F, Haugan H and Brown G J 2004 Effect of interfaces and the spin–orbit band on the band gaps of InAs/GaSb superlattices beyond the standard envelope-function approximation *Phys. Rev.* B **69** 155321

[12] Piquini P, Zunger A and Magri R 2008 Pseudopotential calculations of band gaps and band edges of short-period $(\mathrm{InAs})_n/(\mathrm{GaSb})_m$ superlattices with different substrates, layer orientations, and interfacial bonds *Phys. Rev.* B **77** 115314

[13] Magri R and Zunger A 2002 Effects of interfacial atomic segregation and intermixing on the electronic properties of InAs/GaSb superlattices *Phys. Rev.* B **65** 165302

[14] Lau W H and Flatté M E 2002 Effect of interface structure on the optical properties of InAs/GaSb laser active regions *Appl. Phys. Lett.* **80** 1683–5

[15] Steinshnider J, Harper J, Weimer M, Lin C H, Pei S S, Chow D H 2000 Origin of antimony segregation in GaInSb/InAs strained-layer superlattices *Phys. Rev. Lett.* **85** 4562

[16] Zunger A 2002 On the farsightedness (hyperopia) of the standard k.p model *Phys. Status Solidi* a **190** 467–75

[17] Magri R and Zunger A 2002 Segregation effects on the optical properties of (InAs)/(GaSb) superlattices *Physica* E **13** 325–8

[18] Rodriguez J B, Christol P, Cerutti L, Chevrier F and Joullié A 2005 MBE growth and characterization of type-II InAs/GaSb superlattices for mid-infrared detection *J. Cryst. Growth* **274** 6–13

[19] Ridene S, Debbichi M, Ben Fredj A, Said M and Bouchriha H 2008 Energy-band structure and optical gain in strained InAs(N)/GaSb/InAs(N) quantum well lasers *J. Appl. Phys.* **104** 063706

[20] Debbichi M, Ben Fredj A, Cuminal Y, Lazzari J L, Ridene S, Bouchriha H, Said M and Christol P 2008 InAsN/GaSb/InAsN 'W' quantum well laser for mid-infrared emission: from electronic structure to threshold current density calculations *J. Phys. D: Appl. Phys.* **41** 215106

[21] Cohen A M and Marques G E 1990 Electronic structure of zinc-blende-structure semiconductor heterostructures *Phys. Rev.* B **41** 10608–21

[22] Chuang S L 1995 *Physics of Optoelectronic Devices* (New York: Wiley)

[23] Debbichi M, Ridene S, Bouchriha H, Ben Fredj A, Saïd M, Lazzari J L, Cuminal Y and Christol P 2009 A theoretical study of laser structures based on dilute-nitride InAsN for mid-infrared operation *Semicond. Sci. Technol.* **24** 85010

[24] Debbichi M, Ben Fredj A , Said M, Lazzari J L, Cuminal Y and Christol P 2008 Nitrogen effect on optical gain and radiative current density for mid-infrared InAs(N)/GaSb/InAs(N) quantum-well laser *Physica* E **40** 489–93

[25] Szmulowicz F, Haugan H J, Brown G J, Mahalingam K, Ullrich B, Munshi S R and Grazulis L 2006 Interfaces as design tools for short-period InAs/GaSb type-II superlattices for mid-infrared detectors *Opto-Electron. Rev.* **14** 71